Relightable Neural Actor with Intrinsic Decomposition and Pose Control

Diogo Luvizon[1,2], Vladislav Golyanik[1], Adam Kortylewski[1,3],
Marc Habermann[1,2], Christian Theobalt[1,2]

[1] Max Planck Institute for Informatics, Saarland Informatics Campus

[2] Saarbrücken Research Center for Visual Computing, Interaction and AI [3] University of Freiburg

Project page: https://people.mpi-inf.mpg.de/~dluvizon/relightable-neural-actor/

Figure 1. **Our method learns a neural representation of an actor that is driven only by a 3D skeletal pose and allows rendering and editing of the actor's appearance under new lighting conditions not seen during training.** Our approach models pose-dependent clothing deformations, self-shadows, and provides a new way to map between 3D and UV spaces, enabling the intrinsic decomposition of dynamic sequences. At the same time, our method provides the possibility to easily edit the appearance and material properties at inference time. As input for training, our method only needs a few minutes of multi-view RGB videos and a light environment map.

Abstract

Creating a digital human avatar that is relightable, drivable, and photorealistic is a challenging and important problem in Vision and Graphics. Humans are highly articulated creating pose-dependent appearance effects like self-shadows and wrinkles, and skin as well as clothing require complex and space-varying BRDF models. While recent human relighting approaches can recover plausible material-light decompositions from multi-view video, they do not generalize to novel poses and still suffer from visual artifacts. To address this, we propose Relightable Neural Actor, the first video-based method for learning a photorealistic neural human model that can be relighted, allows appearance editing, and can be controlled by arbitrary skeletal poses. Importantly, for learning our human avatar, we solely require a multi-view recording of the human under a known, but static lighting condition. To achieve this, we represent the geometry of the actor with a drivable density field that models pose-dependent clothing deformations and provides a mapping between 3D and UV space, where normal, visibility, and materials are encoded. To evaluate our approach in real-world scenarios, we collect a new dataset with four actors recorded under different light conditions, indoors and outdoors, providing the first benchmark of its kind for human relighting, and demonstrating state-of-the-art relighting results for novel human poses.

1. Introduction

Creating a relightable and controllable virtual actor of a real person solely from RGB videos is an exciting and challenging topic that has numerous applications in virtual and augmented reality, gaming, human-machine interaction, and content creation. However, intrinsically decomposing the dynamic human geometry, global illumination, and material properties; achieving pose control with realistic dynamic deformations and photoreal relighting effects; and making the problem computationally tractable is still an unsolved problem in research.

Relighting *static* scenes from multi-view imagery is a well-studied problem [17, 26, 39, 49]. However, directly applying such methods to moving humans, which are dynamic, highly articulated, and have complex material composition, is not trivially possible as these approaches do not account for dynamics and their training time ranges from multiple hours to even days, even for a single frame. Despite some works [4, 9, 14, 29] assuming a *well-calibrated lightstage settings*, only few human-specific works [6, 13, 51] try to achieve human intrinsic decomposition and relighting solely *from multi-view video with static lights*. However, at test time, they can solely replay the human motion under novel lighting conditions [6], or do not model global illumination and space-varying BRDF [13], which results in low visual fidelity.

To address this, we propose the first approach that achieves intrinsic decomposition of dynamic human avatars, enabling pose-control and photorealistic rendering, while solely requiring a multi-view video of the real human under a single and static light condition during training (see Fig. 1). At inference time, we only need arbitrary driving skeletal pose and environment map. We solve this challenging problem by modeling the human with an implicit density field controlled via a human body model [27], which provides a pose-driven implicit geometry for arbitrary poses while maintaining a coarse correspondence between points in 3D space and the body model's surface in the respective 2D UV map. In addition, we propose a novel intrinsic decomposition in 2D UV space rather than in 3D space, making the problem computationally tractable for the long and dynamic human sequences. Specifically, we represent normal and visibility information as dynamic maps, and albedo and roughness as static maps. Our key contribution is to sample normal and visibility from the posed geometry and aggregate them into sparse UV maps, which are then densified by the proposed NormalNet and VisibilityNet models. This allows our approach to model wrinkles and self-shadows even for long sequences. The albedo and roughness maps are optimized during training and sampled during rendering. To account for dynamic effects and spurious miss-alignments in the UV projection, this sampling process is guided by the proposed UVDeltaNet, which is intrinsically learned in our pipeline. Finally, given an environment map and a virtual camera position, our neural renderer produces the final image of the neural actor.

To train and evaluate our method, we collected a new real dataset for novel pose and novel lighting human synthesis, composed of four actors recorded under six different light conditions by a multi-view camera setup, including indoor and outdoor environments and a light probe for each sequence, providing the first real in-the-wild benchmark for controllable human relighting. To summarize, our main technical contributions are as follows:

Method	Diffuse	Specular	Pose Control	Dynamic Deform.	Eval. Real Data	Editable
Neural Actor [25]	✘	✘	✔	✔	✔	✘
Relighting4D [6]⋆	✔	✔	✘	✔	✘	✘
RANA [13]†	✔	✘	✔	✘	✘	✘
Ours	✔	✔	✔	✔	✔	✔

⋆ Results do not show specular effects. † Source code not available.

Table 1. Compared to existing approaches, only our method can perform intrinsic decomposition with diffuse and specular effects, model dynamic deformations, and simultaneously supports pose control and editing. Our method is the first to evaluate human relighting numerically under new poses and new lights on real data.

- The first method to learn a relightable neural actor from multi-view RGB videos that allows for pose control, free-viewpoint rendering, diffuse and specular reflection decomposition, and material editing at inference time;
- A new approach to compute dynamic normals and visibility by sparsely sampling a neural field and densifying the results with NormalNet and VisibilityNet, which makes the problem of pose-driven human relighting tractable;
- UVDeltaNet, which accounts for the dynamic effects in UV space, allowing us to learn an explicit and static material representation that is easy to edit at inference time.

In our experimental evaluation, we compare our approach with two baseline variations and show the effectiveness of each component in our method with an ablation study. The quality of our results are extensively illustrated in the paper and in the supplementary materials.

2. Related Work

Relighting a controllable human model with implicit representations is still an open challenge in research. We summarize in Tab. 1 the most related methods, all of which are unable to perform our task under similar assumptions.

2.1. Relighting Static Scenes

Classical approaches for relighting and editing perform intrinsic decomposition through inverse rendering [35]. With recent advances in neural rendering [40], light transportation can be taken into account with fully differentiable rendering pipelines. For instance, Zhang et al. [49] address the problem of recovering geometry and spatially-varying BRDF with an implicit scene representation. However, this requires solving the light transport by evaluating the NeRF model for each light ray, which is very inefficient. NeRV [39] and Zhang et al. [50] mitigate this problem with a neural visibility field that is jointly optimized with the NeRF model, and NeRD [5] adds further relaxation by ignoring cast shadows. However, this assumption cannot be made for humans, which are highly articulated and often experience prominent self-casting shadows. Jin et al. [17] proposes TensorIR, an efficient tensor-based represen-

tation that solves the inverse problem by casting camera- and secondary-rays. IRON [47] proposes a two-stage process for obtaining a mesh with material properties, and Lyu et al. [28] and NeRO [26] focus on multi-bounce illumination and reflective objects, which is usually not the case for humans. A common limitation of these methods is in the assumption of a static scene; therefore, they cannot be trivially adapted to dynamic and controllable humans.

2.2. Human Models with Pose Control

Modeling humans is a long-standing topic. Traditionally, meshes from an actor can be automatically rigged to a skeleton [7] using Linear Blending Skinning (LBS) [21]. Parametric human models offer pose and shape control [27, 33] and, more recently, implicit human bodies can be articulated [3, 30, 31]. Such models offer a generic and controllable representation but are unable to represent individual details. Template-based methods synthesize a realistic level of details [10, 11], but have to deal with non-linear pose-dependent deformations.

Several approaches model appearance and geometry with an implicit field anchored on a coarse human mesh. Neural Body [34] optimizes latent vectors anchored in the vertices of the human mesh and Neural Actor [25] incorporates texture maps as a conditioning to break down the mapping from pose to dynamic effects (one-to-many mapping). ARAH [44] models the surface of the human with an SDF, Dual-Space NeRF [52] learns the color and light in separate spaces, and Kwon et al. [19] propose a generalizable approach. Shysheya et al. [38] jointly learn textures and a neural renderer but fall short in reconstructing the 3D human body. A few works [16, 46] approach a restrictive scenario of reconstructing 3D humans from a monocular video but fail to model fine details under new poses. Common for these methods is the entanglement of material properties and global illumination, making them restricted to the same appearance as observed during training.

2.3. Relighting Human Models

Only a few methods in the literature tackle the problem of relighting humans from video data under static illumination. Li et al. [22] create a relightable human mesh by estimating a low-frequency environment using Spherical Harmonics (SH). Some approaches target the problem of single-image relighting [15] and static pose [51] under unknown lights, which is an extremely ill-posed problem due to the high ambiguity between albedo and lighting. Relighting4D [6] extends Neural Body [34] to estimate geometry and reflectance, but can only replay the same sequence observed during training under new lights and is not able to generate new poses. RANA [13] allows for pose control but assumes Lambertian reflectance, ignoring different material properties such as skin and clothes, and do not model cast shadows, which is a strong limitation for articulated humans.

In contrast, our method performs intrinsic decomposition with space-varying BRDF, models global illumination, allows for pose control and novel lights, and offers an easy manner to edit the material properties of the learned actor.

3. Method

Our goal is to generate a digital human avatar (neural actor) from multi-view RGB images that can be relighted, pose-controlled and rendered from novel viewpoints at test time. We decompose the observed appearance into normals, visibility w.r.t. the light sources, and BRDF represented as albedo and roughness. With these components and an environment map, we employ the microfacet model [42] to render again the observed images. In addition—since we target a drivable actor—the geometry components need to be controllable by the skeletal pose.

Fig. 2 shows an overview of our method divided into three main parts. The first part is a pose-driven geometry model, where the goal is to obtain a skeleton-controllable implicit 3D density field that models the geometry of the actor with pose-dependent deformations. The second part is the new intrinsic decomposition model whose goal is to disentangle geometry represented as normal and visibility information, and material properties as albedo and roughness. Our key insight is to represent these components in UV space rather than in 3D coordinates and use the neural field as a guide in the mapping function between 3D and UV spaces. Finally, we integrate the microfacet model into our rendering pipeline that takes as input the disentangled components (i.e., normal, visibility, albedo, and roughness) and an environment map, and renders the image of the neural actor in an arbitrary pose from a free-viewpoint.

3.1. Inputs and Definitions

Our method takes as input a 3D articulated human skeleton pose $\mathbf{P}_t = \{\boldsymbol{\theta}_t, \mathbf{R}_t, \mathbf{T}_t\}$, defined by the relative joint rotation $\boldsymbol{\theta} \in \mathbb{R}^{J\times 3}$ of J body joints, the global rotation $\mathbf{R} \in \mathbb{R}^{3\times 3}$, and global translation $\mathbf{T} \in \mathbb{R}^3$ of the person at frame t. The 3D pose can be used to drive a coarse human mesh with linear blending skinning (LBS) [27]. We represent the global lights as an environment map $\mathbf{L} \in \mathbb{R}^{16\times 32\times 3}$, which can be obtained from HDR images of a mirror sphere [8]—see the supplement for more details. The environment map can be static during training and changed during inference to render results under novel illumination.

During training, our method is supervised with multi-view calibrated video streams $\mathbf{V}_c = \{\mathbf{I}_{c,t}\}$, where $c \in [1, \dots, C]$ is the camera index and $\mathbf{I}_{c,t}$ is the image from camera c at frame t. We obtain a foreground segmentation mask $\mathbf{M}_{c,t}$ for each video frame [23]. The input 3D skeletons drive the LBS model to obtain posed human meshes

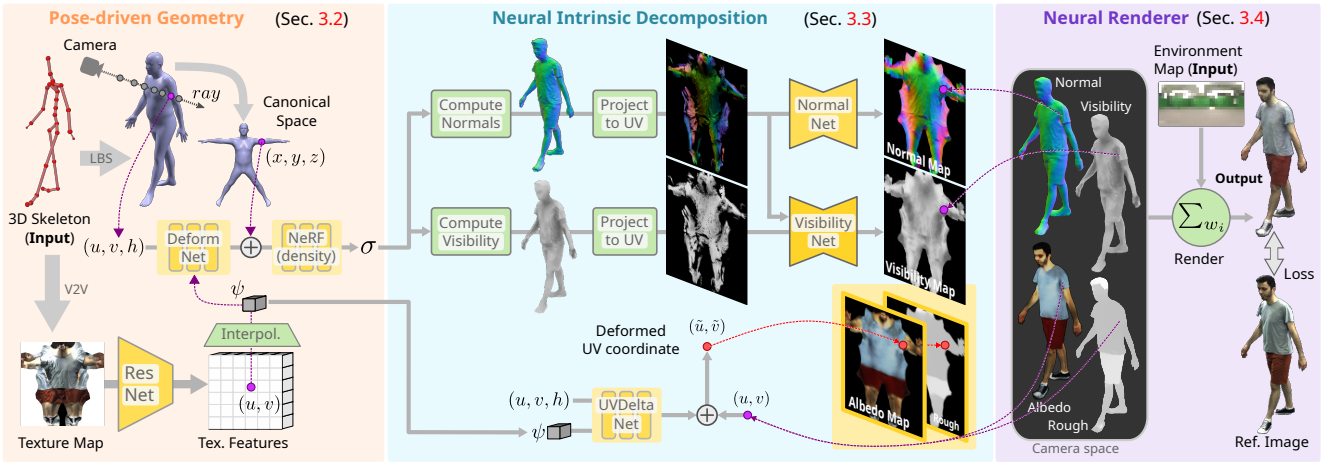

Figure 2. Our method takes as input a 3D skeletal pose and a static environment map, and renders the neural actor from a virtual camera position. The pose-driven geometry (Sec. 3.2) learns an implicit density, from which we can compute normals and visibility. Our intrinsic decomposition disentangles normal, visibility, albedo and roughness maps in UV space (Sec. 3.3). The neural renderer (Sec. 3.4) outputs our prediction, which is supervised with the reference image. Yellow represents learnable components and **green** non-learnable components.

used to extract texture maps from the multi-view images [2]. These texture maps are used during training only. At inference time, they are predicted by a V2V [45] network in a similar way to Neural Actor [25].

3.2. Pose-driven Implicit Human Model

We represent human geometry as an implicit field guided by the skeletal pose parameters $\mathbf{P}_t$. We follow the architecture of Neural Actor [25] and optimize our model through volumetric rendering. However, differently from Liu et al. [25], we sample image patches during training, which allows our method to only process the triangles intersecting the patch region. From each pixel in a patch, we cast rays represented by $\mathbf{r}_n = \mathbf{o} + \delta_n \mathbf{d}$, with origin $\mathbf{o} \in \mathbb{R}^3$ in the optical center of the camera and direction $\mathbf{d} \in \mathbb{R}^3$. Each point in the ray is distant from the camera by the depth value δ_n. The sampled points $\mathbf{r}_n$ are projected to the mesh surface, resulting in the local coordinates (u_n, v_n, h_n), where (u, v) is the surface coordinate in the UV space and h is the signed distance to the mesh. The corresponding points $\mathbf{x}_n = (x, y, z)$ in the canonical space are obtained by unwarping and normalizing the points in world coordinates following the inverse projection of the LSB model.

Next, DeformNet predicts a 3D deformation in the canonical space by taking as input the local coordinates and texture features ψ_n extracted by a ResNet [12] backbone. This is important to model pose-dependent effects, such as wrinkles, that are not modeled by the LBS mesh. Finally, we produce an image

$$\hat{\mathbf{I}}(\mathbf{r}) = \sum_{n=1}^{N} w_n c_n, \quad w_n = T_n \left(1 - \exp\left(-\sigma_n \bar{\delta}_n\right)\right), \quad (1)$$

where $T_n = \exp\left(-\sum_{j=1}^{n-1} \sigma_j \bar{\delta}_j\right)$, w_n is the density weight from standard volumetric rendering [32], $\bar{\delta}_j = \delta_{j+1} - \delta_j$ is the distance between adjacent samples, and c_n and σ_n are the color and density predictions.

Since our goal at this stage is to obtain a drivable high-quality geometry, we only use the image $\hat{\mathbf{I}}$ for supervising the geometry model. The loss for this part is defined as:

$$\mathcal{L}_{\text{geo}} = \lambda_{\text{L2}} \mathcal{L}_{\text{L2}} + \lambda_{\text{vgg}} \mathcal{L}_{\text{vgg}} + \lambda_{\text{hard}} \mathcal{L}_{\text{hard}} + \lambda_{\sigma} \mathcal{L}_{\sigma}, \quad (2)$$

where $\mathcal{L}_{\text{L2}}$ and $\mathcal{L}_{\text{vgg}}$ are the L2 and perceptual losses [20] between $\mathbf{I}$ and $\hat{\mathbf{I}}$, $\mathcal{L}_{\text{hard}}$ is the *hard* loss from Rebain et al. [36], and $\mathcal{L}_{\sigma}$ pushes the density in the empty space to zero. Specifically, the density defined as $\sigma = \text{ReLU}(\sigma')$ suffers from zero-gradient on empty regions and the pre-activated σ' is pushed towards negative values with

$$\mathcal{L}_{\sigma} = (1 - \mathbf{M}(\mathbf{r}))\, \text{sigmoid}(\sigma'), \quad (3)$$

where $\mathbf{M}(\mathbf{r})$ is the binary mask at the pixel intersected by $\mathbf{r}$. $\lambda_{(.)}$ are defined empirically and set to $\lambda_{\text{L2}} = 100$ and $\lambda_{\text{vgg}}{=}\lambda_{\sigma}{=}\lambda_{\text{hard}}{=}0.01$ in all experiments. After training, we discard the color from Eq. (1) and only use the density σ to implicitly represent the geometry of the neural actor.

3.3. Neural Intrinsic Decomposition

We next perform intrinsic decomposition to obtain the normal, visibility, albedo, and roughness components, required for rendering the neural actor under new light conditions. Specifically, for each point in the scene we want to obtain the normal direction $\mathbf{n} \in \mathbb{R}^3$, the soft visibility coefficients $\boldsymbol{v} \in \mathbb{R}^{512}$ respective to the light sources, the RGB albedo $\mathbf{a} \in \mathbb{R}^3$, and the scalar roughness ρ. The normal and visibility values can be obtained from the geometry model. However, computing the visibility of each point in 3D w.r.t. the light sources is computationally intractable for a dynamic and long sequence, since for every point in 3D and for every frame, 512 rays have to be cast towards each pixel of the environment map. Therefore, we use a different approach.

We notice that the intrinsic decomposition is only relevant for points close to the surface. Since the coarse human mesh provides a mapping from the mesh surface to UV space, and our geometry model provides a density field that models the geometry of the actor, we propose an aggregation strategy that samples normal and visibility from a given camera (therefore, only a few points are sampled in 3D) and aggregates the obtained values in a per-frame UV map. We next explain the details of this step.

3.3.1 Normal Maps

For each point in a ray, we want to obtain the normal value that will be required for solving the rendering equation during relighting (will be introduced in Sec. 3.4). This value could be obtained by computing the gradient from the neural field [49]. However, this process requires back-propagating gradients throughout the entire network and often results in noisy normals. Instead, we explicitly compute the normal vector close to the visible surface by leveraging the estimate unbiased depth $\hat{\mathbf{D}}$ [43]:

$$\hat{\mathbf{D}}(\mathbf{r}) = \frac{\sum_{n=1}^{N} w_n \delta_n}{\sum_{n=1}^{N} w_n}. \tag{4}$$

Then, as illustrated in Fig. 3, we convert the depth values relative to the camera to 3D coordinates. The normal direction is obtained by computing the tangent surface at the intersection point. This process can be performed for multiple camera views to cover the surface of the human.

Once the normal values are obtained in 3D, we want to project them to the UV map and aggregate them with the obtained normals from different views. In this process, the (u^*, v^*) coordinate where the obtained normal will be projected to in the UV map is defined by

$$(u^*, v^*) = \underset{(u_n, v_n)}{\arg\max}\, w_n, \tag{5}$$

which corresponds to the (u_n, v_n) value obtained from the point $\mathbf{r}_n$ on the ray that has the largest density weight w_n.

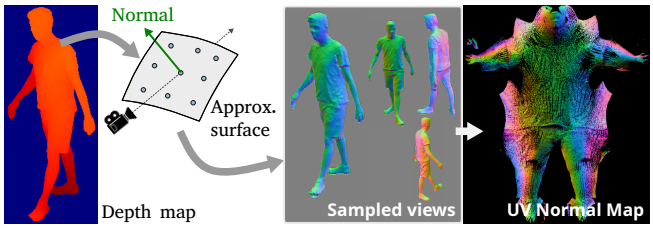

Figure 3. From the obtained unbiased depth from Eq. (4), we project the depth values from camera space to 3D coordinates and approximate the tangent surface at the intersecting point, from which the normal vector is obtained. We sample multiple camera views and aggregate the depth values in UV space.

This process ensures that the obtained normal map aggregates the normals obtained from the regions with the highest probability of being close to the surface.

However, the resulting UV map can be sparse, which is undesirable for free-viewpoint rendering. Thus, the NormalNet is used to inpaint the missing normals in UV space. This lightweight CNN is implemented with 8 layers of partial convolutions [24], takes as input sparse normal maps with size $512 \times 512 \times 3$, and is trained with supervision from densely sampled normal maps from the training data.

3.3.2 Visibility Maps

We make the same assumptions to store visibility information as in the case with the UV representation for normals. However, the visibility for each point in 3D requires querying the neural field thousands of times while casting rays from the intersecting point to all the light sources, which is prohibitive during training. Therefore, we pre-compute the visibility UV maps for each pose by sampling multiple camera views and aggregate the results in UV map following Eq. (5). The resulting sparse visibility maps with size $256 \times 256 \times 512$ are then inpainted by the VisibilityNet (as shown in Fig. 2), which takes as input sparse visibility and normal maps, as the visibility highly depends on normals (e.g. the visibility is always zero for the backlight source), and is trained with densely sampled visibility from the training sequence.

3.3.3 Albedo and Roughness Maps

As discussed above, the normal and visibility components can be directly obtained from the density field. However, the albedo and roughness values cannot be explicitly determined in our setup. In intrinsic decomposition, the material properties are commonly optimized via a differentiable renderer. Hence, we optimize the albedo and roughness of the neural actor by leveraging a differentiable renderer (Sec. 3.4) and by imposing priors through our design.

Assuming that the material properties of an actor should not be dependent on the pose, we model albedo and roughness as static UV maps, respectively defined as $\mathbf{A} \in \mathbb{R}^{1024\times1024\times3}$ and $\mathbf{B} \in \mathbb{R}^{1024\times1024}$. These tensors are jointly optimized for the whole training sequence and regularized with an L1 loss on the spatial gradients, which encourages smoothness in both maps:

$$\mathcal{L}_{\text{smooth}} = \frac{1}{N}\sum |\nabla_x(\mathbf{A})| + |\nabla_y(\mathbf{A})| + |\nabla_x(\mathbf{B})| + |\nabla_y(\mathbf{B})|, \tag{6}$$

where ∇_x and ∇_y represent the spatial gradient operator.

Nonetheless, by assuming a material representation that does not depend on the skeletal pose, we still have to cope with intrinsic mesh registration errors. It is important to mention that, as illustrated in Fig. 2, the human mesh provides guidance to the density field, but also provides the mapping from surface to the UV map. Such registration errors could cause blurry results or artifacts in the final renderings. To cope with this problem, we propose a corrective term to the UV mapping, which is predicted by the UVDeltaNet, as shown in Fig. 2. The UVDeltaNet is an MLP that takes as input the local coordinates (u, v, h) for each point on the ray and the sampled texture features ψ, and outputs a corrective UV term $\epsilon = (u', v')$.

Initially, UVDeltaNet is frozen and outputs zeros. After the initial convergence of $\mathbf{A}$ and $\mathbf{B}$, UVDeltaNet is indirectly supervised by the rendering loss and regularized with:

$$\mathcal{L}_{\text{uv}} = \frac{1}{N}\sum \boldsymbol{\epsilon}^2 + |\nabla_x(\boldsymbol{\epsilon})| + |\nabla_y(\boldsymbol{\epsilon})|, \tag{7}$$

which minimizes the magnitude of the deformation and encourages its spatial gradient to be sparse, i.e., it makes the UV deformation spatially coherent.

3.4. Neural Renderer

The third part of our method is our neural renderer, which takes the disentangled components as normal, visibility, albedo, and rough; integrates the lights from the environment map, and outputs the rendered image.

Based on our volume rendering defined in Sec. 3.2, our neural renderer starts by recasting the ray $\mathbf{r}$ with importance sampling around the estimated depth value $\hat{\mathbf{D}}$. Thus, all the points $\mathbf{r}_n$ are most likely close to the surface. For each sampled point in the ray, we obtain the normal direction $\mathbf{n}_n$ and the visibility $\boldsymbol{\upsilon}_n$ by interpolating the normal and visibility maps in UV around the point (u_n, v_n). The albedo $\mathbf{a}_n$ and roughness ρ_n are obtained by interpolating the albedo and roughness maps in UV around the point $(u_n + u'_u, v_n + v'_n)$.

Before rendering the final image of the neural actor, we consider the light transport equation defined as

$$\mathbf{L}_0(\mathbf{r}_n, \boldsymbol{\omega}_0) = \sum_{\boldsymbol{\omega}_i} \mathrm{R}(\mathbf{a}_n, \rho_n, \boldsymbol{\omega}_i, \boldsymbol{\omega}_0)\boldsymbol{\upsilon}_n\mathbf{L}_i(\boldsymbol{\omega}_i)(\boldsymbol{\omega}_i\mathbf{n}_n), \tag{8}$$

where $\mathrm{R}(\cdot)$ is the microfacet BRDF model [42], $\boldsymbol{\omega}_0$ and $\boldsymbol{\omega}_i$ are the camera and the light source directions, respectively, and $\mathbf{L}_i$ is the incoming light from the environment map. Eq. (8) is defined for a single point $\mathbf{r}_n$ on the ray. We integrate the Eq. (8) in our volume rendering as

$$\tilde{\mathbf{I}}(\mathbf{r}) = \sum_{n=1}^{N} w_n\mathbf{L}_0(\mathbf{r}_n, \boldsymbol{\omega}_0), \tag{9}$$

where $\tilde{\mathbf{I}}$ is the output image of the neural actor.

During training, our relightable model is supervised with the following combined loss:

$$\mathcal{L}_{\text{relight}} = \lambda_{\text{L2}}\mathcal{L}_{\text{L2}} + \lambda_{\text{vgg}}\mathcal{L}_{\text{vgg}} + \lambda_{\text{smooth}}\mathcal{L}_{\text{smooth}} + \mathcal{L}_{\text{uv}}, \tag{10}$$

with $\lambda_{\text{L2}} = 100$, $\lambda_{\text{vgg}} = 0.01$, and $\lambda_{\text{smooth}} = 1$.

4. Relightable Dynamic Actors Dataset

Existing datasets for human reenactment and relighting are often monocular [2, 13], contain very short sequences with only a few pose variations, and do not provide environment maps [2, 13, 25, 34]. Hence, we cannot use them for evaluation under realistic scenarios with real ground truth. In addition, we observe that the only existing synthetic dataset for human relighting and pose control [13] suffers from artifacts in the geometry and salt-and-pepper noise in the renderings; see examples in the supplementary material.

With these shortcomings in mind, we collect a new real dataset, which we call *Relightable Dynamic Actors*, with four identities performing a series of ten different actions. Each subject is recorded six times wearing the same clothes but under different light conditions, including indoor and outdoor, where we used around 100 and eight cameras, respectively. For each sequence, we also capture HDR light probes, which can be used for training or testing. In total, our dataset contains around 90k multi-view video frames divided into 24 multi-view video sequences. See Fig. 4 for samples of our data and the supplement for more details.

5. Experiments

In this section we provide an experimental evaluation of our method on the Relightable Dynamic Actors dataset and show qualitative and quantitative results. Please see the supplementary video for dynamic results.

5.1. Evaluation

Metrics. For quantitative evaluation, we report results on the PSNR, SSIM and LPIPS metrics [48], comparing the rendered relight results with the ground-truth images from our dataset. Importantly, our work is the first to be able to report such metrics on a real dataset since no previous dataset in the literature provided a real human recorded

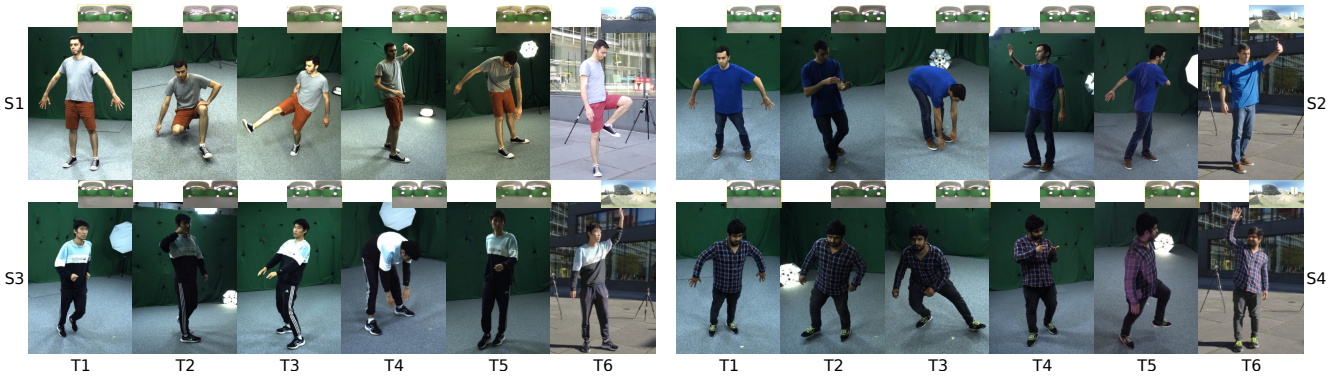

Figure 4. Samples from our *Relightable Dynamic Actors* dataset. For each actor, we recorded six sequences under different light conditions, including five indoor sequences and one outdoor. Light environment maps were computed from HDR pictures of a mirror sphere.

under different and known light conditions. Furthermore, since the only method in the literature capable of reposing a human under new light conditions does not provide implementation [13], we defined two baselines for comparisons.

Baselines. Our two baselines are based on our controllable geometry model (Sec. 3.2) and on the obtained normal and visibility, as discussed in Secs. 3.3.1 and 3.3.2. However, instead of using NormalNet and VisibilityNet to obtain these components, we densely sample the neural field and perform morphological inpainting to obtain dense UV maps. The first baseline, referred to as *Neural Actor+IR*, is an extension of Neural Actor [25] to predict the albedo and rough components instead of RGB color directly from the deformed canonical space $\mathbf{x}_n = (x, y, z)$ (see Fig. 2). The second baseline, *Neural Actor+IR+Tex*, also takes as input the texture features ψ as a conditioning for predicting the albedo and rough values. In both cases, the predictor is a standard NeRF MLP with 8 layers.

Implementation Details. Our model is trained on a three-stage process. First, we train the geometry part (Sec. 3.2) with the Adam [18] optimizer with a learning rate 0.001 until convergence, which takes about two days on four NVidia A40 GPUs. Then, we pre-train the NormalNet and VisibilityNet with pre-compute normal and visibility UV maps sampled from the geometry model from 40 views. Both networks are trained in parallel with Adam and the learning rate of 0.01 for about 12 hours. Finally, we train our intrinsic decomposition model with the same optimizer until convergence, which takes about one day. The predicted texture maps are obtained with a V2V model [45] trained (in parallel to our model) to translate a sequence of SMPL normal maps into a sequence of texture maps. Please refer to our supplementary materials for architecture details.

Figure 5. Qualitative results of our method on novel poses.

Figure 6. Results from our intrinsic decomposition.

5.2. Results

Qualitative results. In Fig. 5, we show qualitative results of our method. Our results are all from a trained model driven by a *new skeletal pose*, *new camera viewpoint*, and *new environment map* not seeing during training. Note how our approach captures realistic appearance and prominent cloth wrinkles, which can be easily observed under different light conditions. Importantly, notice how our results look

Method	T2			T3			T4			T5			T6 (outdoors)		
	PSNR ↑	SSIM ↑	LPIPS ↓	PSNR ↑	SSIM ↑	LPIPS ↓	PSNR ↑	SSIM ↑	LPIPS ↓	PSNR ↑	SSIM ↑	LPIPS ↓	PSNR ↑	SSIM ↑	LPIPS ↓
Neural Actor+IR	17.522	0.750	0.181	17.473	0.768	0.178	17.745	0.767	0.171	18.244	0.768	0.175	18.355	0.710	0.203
Neural Actor+IR+Tex	18.175	0.778	0.164	17.799	0.790	**0.167**	18.132	0.785	0.167	18.531	0.789	0.166	18.704	0.737	0.186
Ours	**18.602**	**0.792**	**0.163**	**18.240**	**0.800**	0.169	**18.388**	**0.800**	**0.164**	**18.820**	**0.800**	**0.165**	**19.461**	**0.753**	**0.173**

Table 2. Quantitative results from our method on real data, subject S1, considering indoor and outdoor scenes. Our method consistently improves the baselines, especially on the outdoor sequence, where the gap between training and test light conditions is more relevant.

Figure 7. Our method models global illumination and cast shadows, as can be observed from our results under "sunrise" light.

Figure 8. Our method offers the possibility to edit the material properties and simultaneously perform skeletal pose control, free-viewpoint rendering, and relighting of the edited neural actor.

realistic under novel light conditions.

In Fig. 6, we show results from our intrinsic decomposition. Note how our normal representation captures well the geometry details, and how our visibility captures shadows. This is important to obtain an albedo that does not embed light effects, as can be observed from our results. Another important and unique characteristic of our method is the ability to model self-shadows. In Fig. 7, we show results from two subjects, where a "sunrise" environment map was used to produce cast shadows.

Comparisons. We evaluated our method on the test sequences from our dataset. Specifically, we compare with two baselines in the indoor sequences (T2-T5) and outdoor sequence (T6) of subject S1 in every 10th frame, which sums up to 4000 evaluation frames. In Tab. 2 we show, for the first time, quantitative results of real human relighting under new poses and new light conditions. Our approach consistently improves upon the two baselines.

Ablation. We show in Tab. 3 an ablation with different components of our method. Compared to our baseline (Neural Actor+IR), learning the albedo and roughness as UV maps significantly improves the performance on relighting and reposing. This is because, in the baselines, the albedo and roughness are under-constrained and can possibly embed shading effects, overfiting to the training data. The NormalNet and VisiblityNet provide additional capacity to the model to learn how to inpaint the sampled UV maps. Note that without these two models our results are computed using morphological region growth in the UV maps. Finally, the UVDeltaNet provides more flexibility to the albedo and roughness representation, accounting for fine details. This can be observed in the improvement in the LPIPS metric in the last row of Tab. 3. Nonetheless, this also means more capacity to overfit the training sequences, which translates into a small decrease in the PSNR metric.

Method	Indoors (S1,T2)			Outdoors (S1,T6)		
	PSNR ↑	SSIM ↑	LPIPS ↓	PSNR ↑	SSIM ↑	LPIPS ↓
Baseline	17.522	0.750	0.181	18.355	0.710	0.203
+Albedo/Rough Maps	18.334	0.789	0.168	19.341	0.747	0.181
+Normal/Vis.Net	**18.634**	**0.792**	0.173	**19.704**	**0.760**	0.180
+UVDeltaNet (**Ours**)	18.602	**0.792**	**0.163**	19.461	0.753	**0.173**

Table 3. Ablation study with different components of our method.

5.3. Applications

An important characteristic of our approach is our static representation in UV for the albedo and roughness. This allows exciting and new applications such as color and material editing of an animatable and relightable neural actor, as shown in Fig. 8 and in Fig. 1. With a simple edit in the obtained albedo or roughness 2D map, we can insert new textures or new materials and render the edited neural actor under new poses, new viewpoints, and new light conditions.

6. Conclusion

We conclude that the proposed method for the free-viewpoint rendering of humans enables simultaneous relighting, material editing, and pose control at test time with unprecedented quality and level of detail. Our method demonstrates functionality that no competing method making the same assumptions at training time (i.e. from multi-view RGB video inputs only) can provide. We hope that our method and the proposed dataset will provoke further

research in this exciting field, bringing the neural rendering of humans to a new qualitative level and paving the way for next-generation metaverse applications.

Limitations. This work focuses on visual fidelity, and representations faster than NeRF could be tested in our framework in future. Moreover, like several previous techniques for the free-viewpoint rendering of humans and avatar generation [25, 37], the proposed method can currently only deal with tight clothing due to the coarse geometry registration.

References

[1] Easymocap - make human motion capture easier. Github, 2021. 2

[2] Thiemo Alldieck, Marcus Magnor, Weipeng Xu, Christian Theobalt, and Gerard Pons-Moll. Video based reconstruction of 3d people models. In *Computer Vision and Pattern Recognition (CVPR)*, pages 8387–8397, 2018. 4, 6

[3] Thiemo Alldieck, Hongyi Xu, and Cristian Sminchisescu. imghum: Implicit generative models of 3d human shape and articulated pose. In *International Conference on Computer Vision (ICCV)*, pages 5461–5470, 2021. 3

[4] Sai Bi, Stephen Lombardi, Shunsuke Saito, Tomas Simon, Shih-En Wei, Kevyn Mcphail, Ravi Ramamoorthi, Yaser Sheikh, and Jason Saragih. Deep relightable appearance models for animatable faces. *ACM Transactions on Graphics (TOG)*, 40(4):1–15, 2021. 2

[5] Mark Boss, Raphael Braun, Varun Jampani, Jonathan T Barron, Ce Liu, and Hendrik Lensch. Nerd: Neural reflectance decomposition from image collections. In *International Conference on Computer Vision (ICCV)*, pages 12684–12694, 2021. 2

[6] Zhaoxi Chen and Ziwei Liu. Relighting4d: Neural relightable human from videos. In *ECCV*, 2022. 2, 3

[7] Edilson De Aguiar, Christian Theobalt, Sebastian Thrun, and Hans-Peter Seidel. Automatic conversion of mesh animations into skeleton-based animations. In *Computer Graphics Forum (EUROGRAPHICS)*, pages 389–397, 2008. 3

[8] Paul E Debevec and Jitendra Malik. Recovering high dynamic range radiance maps from photographs. In *ACM SIGGRAPH 2008 classes*, pages 1–10. 2008. 3, 2

[9] Kaiwen Guo, Peter Lincoln, Philip Davidson, Jay Busch, Xueming Yu, Matt Whalen, Geoff Harvey, Sergio Orts-Escolano, Rohit Pandey, Jason Dourgarian, et al. The relightables: Volumetric performance capture of humans with realistic relighting. *ACM Transactions on Graphics (ToG)*, 38(6):1–19, 2019. 2

[10] Marc Habermann, Weipeng Xu, Michael Zollhoefer, Gerard Pons-Moll, and Christian Theobalt. Livecap: Real-time human performance capture from monocular video. *ACM Transactions On Graphics (TOG)*, 38(2):1–17, 2019. 3

[11] Marc Habermann, Weipeng Xu, Michael Zollhofer, Gerard Pons-Moll, and Christian Theobalt. Deepcap: Monocular human performance capture using weak supervision. In *Proceedings of the IEEE/CVF Conference on Computer Vision and Pattern Recognition*, pages 5052–5063, 2020. 3

[12] Kaiming He, Xiangyu Zhang, Shaoqing Ren, and Jian Sun. Deep residual learning for image recognition. In *Conference on Computer Vision and Pattern Recognition (CVPR)*, pages 770–778, 2016. 4

[13] Umar Iqbal, Akin Caliskan, Koki Nagano, Sameh Khamis, Pavlo Molchanov, and Jan Kautz. Rana: Relightable articulated neural avatars. In *International Conference on Computer Vision (ICCV)*, pages 23142–23153, 2023. 2, 3, 6, 7

[14] Shun Iwase, Shunsuke Saito, Tomas Simon, Stephen Lombardi, Timur Bagautdinov, Rohan Joshi, Fabian Prada, Takaaki Shiratori, Yaser Sheikh, and Jason Saragih. Relightablehands: Efficient neural relighting of articulated hand models. In *Proceedings of the IEEE/CVF Conference on Computer Vision and Pattern Recognition*, pages 16663–16673, 2023. 2

[15] Chaonan Ji, Tao Yu, Kaiwen Guo, Jingxin Liu, and Yebin Liu. Geometry-aware single-image full-body human relighting. In *European Conference on Computer Vision (ECCV)*, pages 388–405. Springer, 2022. 3

[16] Wei Jiang, Kwang Moo Yi, Golnoosh Samei, Oncel Tuzel, and Anurag Ranjan. Neuman: Neural human radiance field from a single video. In *European Conference on Computer Vision (ECCV)*, pages 402–418, 2022. 3

[17] Haian Jin, Isabella Liu, Peijia Xu, Xiaoshuai Zhang, Songfang Han, Sai Bi, Xiaowei Zhou, Zexiang Xu, and Hao Su. Tensoir: Tensorial inverse rendering. In *Computer Vision and Pattern Recognition (CVPR)*, pages 165–174, 2023. 2

[18] Diederik P Kingma and Jimmy Ba. Adam: A method for stochastic optimization. *arXiv preprint arXiv:1412.6980*, 2014. 7

[19] Youngjoong Kwon, Dahun Kim, Duygu Ceylan, and Henry Fuchs. Neural human performer: Learning generalizable radiance fields for human performance rendering. *Advances in Neural Information Processing Systems (NeurIPS)*, 34: 24741–24752, 2021. 3

[20] Christian Ledig, Lucas Theis, Ferenc Huszár, Jose Caballero, Andrew Cunningham, Alejandro Acosta, Andrew Aitken, Alykhan Tejani, Johannes Totz, Zehan Wang, et al. Photo-realistic single image super-resolution using a generative adversarial network. In *Computer Vision and Pattern Recognition (CVPR)*, pages 4681–4690, 2017. 4

[21] J. P. Lewis, Matt Cordner, and Nickson Fong. Pose space deformation: A unified approach to shape interpolation and skeleton-driven deformation. In *SIGGRAPH*, page 165–172, USA, 2000. ACM Press/Addison-Wesley Publishing Co. 3

[22] Guannan Li, Chenglei Wu, Carsten Stoll, Yebin Liu, Kiran Varanasi, Qionghai Dai, and Christian Theobalt. Capturing relightable human performances under general uncontrolled illumination. In *Computer Graphics Forum*, pages 275–284. Wiley Online Library, 2013. 3

[23] Shanchuan Lin, Andrey Ryabtsev, Soumyadip Sengupta, Brian L Curless, Steven M Seitz, and Ira Kemelmacher-Shlizerman. Real-time high-resolution background matting. In *Computer Vision and Pattern Recognition (CVPR)*, pages 8762–8771, 2021. 3

[24] Guilin Liu, Fitsum A. Reda, Kevin J. Shih, Ting-Chun Wang, Andrew Tao, and Bryan Catanzaro. Image inpainting for ir-

regular holes using partial convolutions. In *The European Conference on Computer Vision (ECCV)*, 2018. 5, 1

[25] Lingjie Liu, Marc Habermann, Viktor Rudnev, Kripasindhu Sarkar, Jiatao Gu, and Christian Theobalt. Neural actor: Neural free-view synthesis of human actors with pose control. *ACM Transactions on Graphics (TOG)*, 40(6):1–16, 2021. 2, 3, 4, 6, 7, 9, 1

[26] Yuan Liu, Peng Wang, Cheng Lin, Xiaoxiao Long, Jiepeng Wang, Lingjie Liu, Taku Komura, and Wenping Wang. Nero: Neural geometry and brdf reconstruction of reflective objects from multiview images. In *SIGGRAPH*, 2023. 2, 3

[27] Matthew Loper, Naureen Mahmood, Javier Romero, Gerard Pons-Moll, and Michael J. Black. SMPL: A skinned multi-person linear model. *ACM Transactions on Graphics (SIGGRAPH Asia)*, 34(6):248:1–248:16, 2015. 2, 3

[28] Linjie Lyu, Ayush Tewari, Thomas Leimkuehler, Marc Habermann, and Christian Theobalt. Neural radiance transfer fields for relightable novel-view synthesis with global illumination. In *ECCV*, 2022. 3

[29] Abhimitra Meka, Rohit Pandey, Christian Häne, Sergio Orts-Escolano, Peter Barnum, Philip David-Son, Daniel Erickson, Yinda Zhang, Jonathan Taylor, Sofien Bouaziz, Chloe Legendre, Wan-Chun Ma, Ryan Overbeck, Thabo Beeler, Paul Debevec, Shahram Izadi, Christian Theobalt, Christoph Rhemann, and Sean Fanello. Deep relightable textures: Volumetric performance capture with neural rendering. *ACM Trans. Graph.*, 39(6), 2020. 2

[30] Marko Mihajlovic, Yan Zhang, Michael J Black, and Siyu Tang. Leap: Learning articulated occupancy of people. In *Proceedings of the IEEE/CVF Conference on Computer Vision and Pattern Recognition*, pages 10461–10471, 2021. 3

[31] Marko Mihajlovic, Shunsuke Saito, Aayush Bansal, Michael Zollhoefer, and Siyu Tang. COAP: Compositional articulated occupancy of people. In *Computer Vision and Pattern Recognition (CVPR)*, 2022. 3

[32] Ben Mildenhall, Pratul P. Srinivasan, Matthew Tancik, Jonathan T. Barron, Ravi Ramamoorthi, and Ren Ng. Nerf: Representing scenes as neural radiance fields for view synthesis. In *ECCV*, 2020. 4, 1

[33] Georgios Pavlakos, Vasileios Choutas, Nima Ghorbani, Timo Bolkart, Ahmed A. A. Osman, Dimitrios Tzionas, and Michael J. Black. Expressive body capture: 3d hands, face, and body from a single image. In *Computer Vision and Pattern Recognition (CVPR)*, 2019. 3

[34] Sida Peng, Yuanqing Zhang, Yinghao Xu, Qianqian Wang, Qing Shuai, Hujun Bao, and Xiaowei Zhou. Neural body: Implicit neural representations with structured latent codes for novel view synthesis of dynamic humans. In *CVPR*, 2021. 3, 6

[35] Ravi Ramamoorthi and Pat Hanrahan. A signal-processing framework for inverse rendering. In *Conference on Computer Graphics and Interactive Techniques*, page 117–128, New York, NY, USA, 2001. Association for Computing Machinery. 2

[36] Daniel Rebain, Mark Matthews, Kwang Moo Yi, Dmitry Lagun, and Andrea Tagliasacchi. Lolnerf: Learn from one look. In *Computer Vision and Pattern Recognition (CVPR)*, pages 1558–1567, 2022. 4

[37] Edoardo Remelli, Timur Bagautdinov, Shunsuke Saito, Chenglei Wu, Tomas Simon, Shih-En Wei, Kaiwen Guo, Zhe Cao, Fabian Prada, Jason Saragih, et al. Drivable volumetric avatars using texel-aligned features. In *ACM SIGGRAPH 2022 Conference Proceedings*, 2022. 9

[38] Aliaksandra Shysheya, Egor Zakharov, Kara-Ali Aliev, Renat Bashirov, Egor Burkov, Karim Iskakov, Aleksei Ivakhnenko, Yury Malkov, Igor Pasechnik, Dmitry Ulyanov, et al. Textured neural avatars. In *Proceedings of the IEEE/CVF Conference on Computer Vision and Pattern Recognition*, pages 2387–2397, 2019. 3

[39] P. P. Srinivasan, B. Deng, X. Zhang, M. Tancik, B. Mildenhall, and J. T. Barron. Nerv: Neural reflectance and visibility fields for relighting and view synthesis. In *Computer Vision and Pattern Recognition (CVPR)*, pages 7491–7500, 2021. 2

[40] A. Tewari, J. Thies, B. Mildenhall, P. Srinivasan, E. Tretschk, W. Yifan, C. Lassner, V. Sitzmann, R. Martin-Brualla, S. Lombardi, T. Simon, C. Theobalt, M. Nießner, J. T. Barron, G. Wetzstein, M. Zollhöfer, and V. Golyanik. Advances in Neural Rendering. *Computer Graphics Forum (EG STAR 2022)*, 2022. 2

[41] TheCaptury. The Captury. http://www.thecaptury.com/, 2020. 2

[42] Bruce Walter, Stephen R. Marschner, Hongsong Li, and Kenneth E. Torrance. Microfacet Models for Refraction through Rough Surfaces. In *Rendering Techniques*. The Eurographics Association, 2007. 3, 6

[43] Peng Wang, Lingjie Liu, Yuan Liu, Christian Theobalt, Taku Komura, and Wenping Wang. Neus: Learning neural implicit surfaces by volume rendering for multi-view reconstruction. In *Advances in Neural Information Processing Systems*, 2021. 5

[44] Shaofei Wang, Katja Schwarz, Andreas Geiger, and Siyu Tang. Arah: Animatable volume rendering of articulated human sdfs. In *European Conference on Computer Vision (ECCV)*, 2022. 3

[45] Ting-Chun Wang, Ming-Yu Liu, Jun-Yan Zhu, Guilin Liu, Andrew Tao, Jan Kautz, and Bryan Catanzaro. Video-to-video synthesis. In *Conference on Neural Information Processing Systems (NeurIPS)*, 2018. 4, 7

[46] Chung-Yi Weng, Brian Curless, Pratul P. Srinivasan, Jonathan T. Barron, and Ira Kemelmacher-Shlizerman. Humannerf: Free-viewpoint rendering of moving people from monocular video. In *Conference on Computer Vision and Pattern Recognition (CVPR)*, pages 16210–16220, 2022. 3

[47] Kai Zhang, Fujun Luan, Zhengqi Li, and Noah Snavely. IRON: Inverse rendering by optimizing neural sdfs and materials from photometric images. In *Proceedings of the IEEE/CVF Conference on Computer Vision and Pattern Recognition*, pages 5565–5574, 2022. 3

[48] Richard Zhang, Phillip Isola, Alexei A Efros, Eli Shechtman, and Oliver Wang. The unreasonable effectiveness of deep features as a perceptual metric. In *CVPR*, 2018. 6

[49] Xiuming Zhang, Pratul P Srinivasan, Boyang Deng, Paul Debevec, William T Freeman, and Jonathan T Barron. NeRFactor: Neural factorization of shape and reflectance under an unknown illumination. *ACM Transactions on Graphics (TOG)*, 40:1–18, 2021. 2, 5

[50] Yuanqing Zhang, Jiaming Sun, Xingyi He, Huan Fu, Rongfei Jia, and Xiaowei Zhou. Modeling indirect illumination for inverse rendering. In *Proceedings of the IEEE/CVF Conference on Computer Vision and Pattern Recognition*, pages 18643–18652, 2022. 2

[51] Ruichen Zheng, Peng Li, Haoqian Wang, and Tao Yu. Learning visibility field for detailed 3d human reconstruction and relighting. In *Computer Vision and Pattern Recognition (CVPR)*, pages 216–226, 2023. 2, 3

[52] Yihao Zhi, Shenhan Qian, Xinhao Yan, and Shenghua Gao. Dual-space nerf: Learning animatable avatars and scene lighting in separate spaces. *arXiv preprint arXiv:2208.14851*, 2022. 3

Relightable Neural Actor with Intrinsic Decomposition and Pose Control

Supplementary Material

This document accompanies our paper "Relightable Neural Actor with Intrinsic Decomposition and Pose Control" and includes additional implementation details on the network architectures (Sec. 7) and dataset collection (Sec. 8). The dynamic results of our method are provided in the supplementary video.

7. Network Architectures

7.1. Pose-driven Geometry Model

The neural network architecture of our pose-driven geometry model is implemented based on Neural Actor [25] and is illustrated in Fig. 9. The RGB color output c is activated with the *sigmoid* function, and the density output σ is activated with ReLU. The yellow rectangular blocks represent a single fully connected layer.

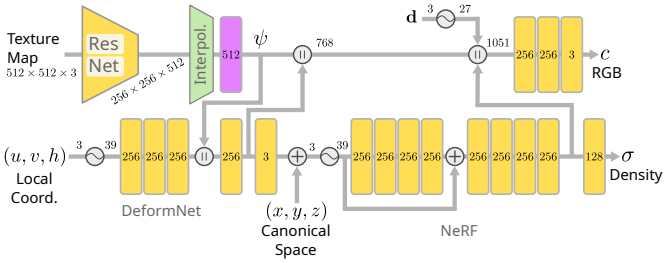

Figure 9. Neural network architecture of our pose-driven geometry model. The RGB color branch is only used during the training phase of the geometry model and is discarded during the relighting training and inference. The interpolation of texture features (obtained from the texture map) is performed in the UV coordinate (u, v) given by the projection of 3D points to the human mesh, as introduced in Sec. 3.2. The obtained feature vector ψ (represented in purple) is also used in our UVDeltaNet. The symbol "$\sim$"refers to positional encoding as in NeRF [32] and "||" refers to feature-wise concatenation.

7.2. NormalNet Model

The goal of NormalNet in our approach is to perform inpainting and refinement of the normal values sampled from the neural field and aggregated in the UV map. Therefore, we leverage partial convolutions [24] as a building block and design a shallow convolutional neural network (CNN) that is shown in Fig. 10.

7.3. VisibilityNet Model

We use a similar approach as in the NormalNet architecture for inpainting and refining the visibility information. However, the visibility is highly dependent on the normal values, since half of the light sources in the environment map are back lit as a function of the normal direction. Therefore, the VisibilityNet model also takes as input the sampled normal maps. The shallow CNN architecture of VisibilityNet is shown in Fig. 11.

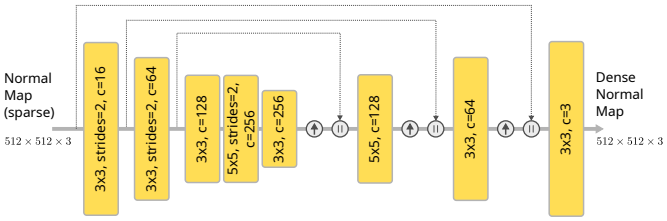

Figure 10. Neural network architecture of our NormalNet model. Each rectangular block is a 2D partial convolution. Binary masks are applied to all the feature maps and to the input, as defined in Liu et al. [24]. The symbol "↑" refers to depth-to-space transformation, where the spatial resolution is increased by a factor of 2 in each dimension, and "||" refers to feature-wise concatenation.

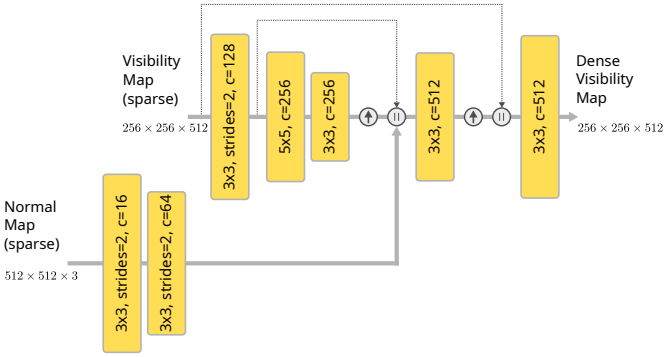

Figure 11. Neural network architecture of our VisibilityNet model. Rectangular blocks represent 2D partial convolutions. "↑" and "||" refer to depth-to-space transformation and feature-wise concatenation, respectively.

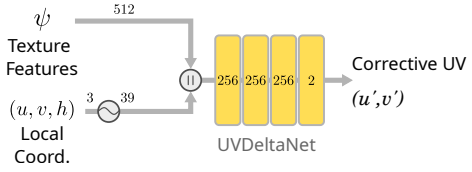

Figure 12. Neural network architecture of our UVDeltaNet model.

7.4. UVDeltaNet Model

The architecture of UVDeltaNet, introduced in Sec. 3.3.3, is shown in Fig. 12. This shallow MLP has as objective predict a corrective term in UV space, therefore, it takes as input the local coordinates (u, v, h) and the texture features ψ (see Fig. 9), and predicts a corrective term (u', v').

8. Dataset Collection

We collected our dataset "Relightable Dynamic Actors" with the goal to provide a real dataset with the same person recorded under different light conditions. For each sequence, the actors were instructed to follow a sequence of 10 activities defined as: *stretch arms*, *walk in a circle*, *jogging*, *stretch legs*, *talk on the phone*, *use a tablet*, *stretch legs up*, *stretch back*, *wave hands*, *freestyle*. We use a commercial markerless motion tracking system [41] for obtaining the human motion in 3D from the calibrated multi-view videos. To fit SMPL model [27] to our tracking, we first optimize the pose and shape parameters in the rest pose "T-pose" with a 3D body joint loss between SMPL and the tracked 3D pose based on EasyMocap [1].

We obtained the environment map for each sequence by taking multi-exposure pictures from a mirror sphere. The HDR image of the mirror sphere was obtained with the algorithm from Debevec and Malik [8]. We combined two shots of the mirror sphere from different angles. The combined image was unwrapped to the EXR latitude-longitude format, resulting in the HDR environment map. Two samples from our environment maps are shown in Fig. 13.

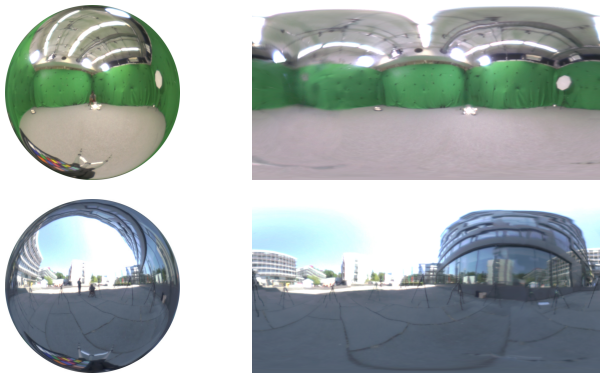

Figure 13. Samples from our environment maps obtained from indoor and outdoor sequences. On the left is the light probe obtained with HDR pictures from a mirror sphere and on the right is the processed HDR images converted to a latitude-longitude format (EXR). The environment maps (right) are then resized to 32×16 pixels to be used in our method.